Three-dimensional flow instability in a lid-driven isosceles triangular cavity

L. M. GONZÁLEZ[1]†, M. AHMED[2], J. KÜHNEN[2], H. C. KUHLMANN[2]† AND V. THEOFILIS[3]

[1]School of Naval Engineering, Universidad Politécnica de Madrid, Pza. Cardenal Cisneros 3, E-28040 Madrid, Spain

[2]Institute of Fluid Mechanics and Heat Transfer, Vienna University of Technology, Resselgasse 3/1/2, A-1040 Vienna, Austria

[3]School of Aeronautics, Universidad Politécnica de Madrid, Pza. Cardenal Cisneros 3, E-28040 Madrid, Spain

Linear three-dimensional modal instability of steady laminar two-dimensional states developing in a lid-driven cavity of isosceles triangular cross-section is investigated theoretically and experimentally for the case in which the equal sides form a rectangular corner. An asymmetric steady two-dimensional motion is driven by the steady motion of one of the equal sides. If the side moves away from the rectangular corner, a stationary three-dimensional instability is found. If the motion is directed towards the corner, the instability is oscillatory. The respective critical Reynolds numbers are identified both theoretically and experimentally. The neutral curves pertinent to the two configurations and the properties of the respective leading eigenmodes are documented and analogies to instabilities in rectangular lid-driven cavities are discussed.

Key words: instability, transition to turbulence

1. Introduction

Flow in lid-driven cavities has occupied fluid mechanics research for decades, both from a theoretical/numerical and from an experimental point of view. Unlike flow and flow instability in simpler square and rectangular containers, which are now fairly well understood, relatively less work is presently available in three-dimensional lid-driven cavities of complex two-dimensional cross-sectional shapes. The present contribution addresses, from a theoretical and an experimental point of view, three-dimensional flow instability in the canonical lid-driven cavity of isosceles triangular cross-section. The reader interested in a full review of internal re-circulating flows generated by the motion of one or more of the container walls is referred to Shankar & Deshpande (2000), who discuss issues such as corner eddies, longitudinal vortices, non-uniqueness, transition and turbulence, as understood up to the point in time in which that article was written. Here, a short review of known and newer results is presented, in order to place the present work in the appropriate context.

The first numerical solution of a square lid-driven cavity flow was obtained in the early 60s of last century, in the Reynolds number range 0–64, by Kawaguti (1961). An extension to rectangular cavities was accomplished by Simuni (1965), who solved the unsteady Navier–Stokes equations up to $Re = 1000$. In his now classic work, Burggraf (1966) discussed the convergence of the latter solutions and demonstrated that they were under-resolved at $Re > 400$. He went on to provide the first accurate solutions of the two-dimensional equations of motion in a square domain up to $Re = 400$ and used the results to discuss the earlier theories of Batchelor (1956) and Moffat (1963), respectively regarding the development of the centre vortex in the limit $Re \to \infty$ and corner vortices at finite Reynolds numbers. The experimental work of Pan & Acrivos (1967) presented flow visualization results at finite aspect ratio cavities in the Reynolds number range $Re = 20$–4000 and discussed the distribution of viscous and inertia forces as a function of the depth of the cavity and the Reynolds number. By far the most quoted two-dimensional numerical simulations of square lid-driven cavity flow are those of Ghia, Ghia & Shin (1982) and Schreiber & Keller (1983), who extended the range of solutions obtained to $Re \leqslant 10\,000$, while the square lid-driven cavity problem continued to serve as benchmark for numerical solutions of the incompressible equations of motion during that decade and beyond (e.g. Luchini 1991).

Unsteadiness observed in numerical solutions of flow in the strictly two-dimensional rectangular cavity, as well as unsteadiness and transition to three-dimensional flow recovered both experimentally and numerically in three-dimensional, spanwise homogeneous flow in a container of rectangular cross-section, are now fairly well-understood in the context of linear global flow instability (Theofilis 2011). Regarding Hopf bifurcations in the square cavity restricted to two-dimensional flow, the interested reader is referred to the work of Poliashenko & Aidun (1995), as well as to the more recent contribution of Boppana & Gajjar (2010) and the related discussion of Brezillon, Girault & Cadou (2010). To date, the range of linear critical Reynolds numbers predicted for two-dimensional (spanwise wavenumber parameter $k = 0$) global flow instability, $Re_{2d,crit} \in [7400, 8375]$, is wide enough to warrant further work. As far as three-dimensional global instability of spanwise homogeneous square lid-driven cavity flows is concerned, the analysis of Ding & Kawahara (1998) as well as the independently obtained complete parametric studies of three-dimensional instability in the square cavity by Theofilis (2000) and Albensoeder, Kuhlmann & Rath (2001*b*) are mentioned. The first work provided an accurate description of the third unstable mode of the flow, while the second and third works completed the instability map of the flow by discovering independently the leading eigenmode of the flow, stationary mode S1 with critical parameters ($Re_c^{\omega=0} \approx 783, k_c^{\omega=0} \approx 15.4$) and the three additional travelling neutral modes, T1, T2 and T3, at ($Re_{n2}^{\omega\neq 0} \approx 845, k_{n2}^{\omega\neq 0} \approx 15.8$), ($Re_{n3}^{\omega\neq 0} \approx 922, k_{n3}^{\omega\neq 0} \approx 7.4$) and ($Re_{n4}^{\omega\neq 0} \approx 961, k_{n4}^{\omega\neq 0} \approx 14.3$), respectively. In the latter work, a complete study of the effect of aspect ratio is also presented. By contrast to the wide range of critical conditions of two-dimensional flow instability, substantially better agreement exists in the literature regarding the minima of the first four neutral modes of three-dimensional square lid-driven cavity.

Still within the context of two-dimensional rectangular domains, an interesting extension of the classical rectangular lid-driven cavity flow is that in which two facing walls are permitted to move tangentially in opposite directions. Albensoeder, Kuhlmann & Rath (2001*a*) found several saddle-node bifurcations of the two-dimensional steady flow leading to non-uniqueness. Their work was preceded by Kuhlmann, Wanschura & Rath (1997) who performed numerical and experimental investigations, which delivered both stationary base flows under variation of the

cavity aspect ratio and the two Reynolds numbers associated with the moving walls; both in their experiments and in the associated theoretical work, the basic flow is considered homogeneous along the third spatial direction. Subsequently, a global instability analysis delivered the critical conditions as a function of these parameters. In subsequent investigations, Albensoeder & Kuhlmann (2002*a*,*b*) investigated the linear stability boundaries as functions of the two Reynolds numbers and the aspect ratio, finally establishing the complete linear stability balloon (Albensoeder & Kuhlmann 2003).

Further experimentation and a discussion of the different classes of instabilities in the rectangular two-lid driven cavity have been provided by Siegmann-Hegerfeld, Albensoeder & Kuhlmann (2008), who documented the stability boundaries of the two-dimensional steady flows and established a close correspondence between linear stability calculations and detailed laser Doppler velocimetry (LDV) measurements. Another extension of the classic lid-driven cavity work is the experimental and numerical study of Humphrey *et al.* (2003), who visualized and computed shear-driven incompressible flow in a toroidal cavity of square cross-section; three-dimensional structures were identified, reminiscent of those associated with global three-dimensional instability in the simpler cavity flows, although no analysis was performed in the context of the latter work. The sensitivity of lid-driven cavity flows in rectangular containers driven by motion of one or two opposite lids has been analysed by Giannetti, Luchini & Marino (2010) using adjoint-based analysis (Hill 1992, 1995), which delivers the region of the flow where the global mode is most sensitive to localized initial perturbations.

Three-dimensional rectangular cavities have received attention mainly from an experimental point of view, while benchmark direct numerical simulation results have been produced in the cubic cavity; in the last year, linear instability analyses in the cubic cavity geometry have also appeared in the literature. Early experimental results in three-dimensional cavities were presented by Koseff *et al.* (1983), Koseff & Street (1984*a*), Rhee, Koseff & Street (1984) and Prasad & Koseff (1989), all at Reynolds numbers $Re = O(10^3)$. Consistently, it was found that longitudinal Taylor–Görtler-like (TGL) vortices appear as the first three-dimensional flow structure when the Reynolds number is increased, a phenomenon that was associated qualitatively with centrifugal instability. The size of the TGL vortices was found to scale with the boundary layer thickness, which is usually small compared to the linear dimensions of the container. When the Reynolds number is increased, these vortices become time-dependent and start to meander (Koseff & Street 1984*b*). The geometry addressed experimentally by Aidun, Triantafillopoulos & Benson (1991) is a three-dimensional rectangle with height-to-width aspect ratio of $\Gamma = h/d = 1$ and span-to-width ratio $A = l/d = 3$, where h, d and l are the height, width, and span of the cavity, respectively. In this work too, spanwise cells were observed and a complete study of their distribution pattern was performed, varying the flow Reynolds number between the limits $500 \leqslant Re \leqslant 2000$; the propagation of the spiral waves along the secondary downstream eddy was also documented.

From a numerical point of view, early three-dimensional direct numerical simulations of flow in the cubic lid-driven cavity include the works of Freitas *et al.* (1985), at $Re \leqslant 3200$, Ku, Hirsch & Taylor (1987), at $Re \leqslant 1000$ and Deville, Le & Morchoisne (1992), also at $Re = 3200$. Guj & Stella (1993) also presented cubical three-dimensional lid-driven cavity solutions at $Re \in [400, 3200]$. Recent direct numerical simulations of three-dimensional rectangular lid-driven cavity flows at $Re = 10^3$ have been presented by Albensoeder & Kuhlmann (2006), who studied

the effect of spanwise aspect ratio, as well as that of spanwise confinement versus spanwise periodicity of the flow. Significant increases in the Reynolds number range studied in a cubical lid-driven cavity were accomplished in the works of Verstappen & Veldman (1994) and Leriche & Gavrilakis (2000), who simulated both steady and unsteady flows at $Re = 10\,000$ and $Re \leqslant 12\,000$, respectively. The results obtained revealed that the flow is laminar over most of the domain, with distinct wall-jet profiles identifiable in three of the cavity walls. Finally, Leriche (2006) has performed high-Reynolds-number direct numerical simulations in the same cubical lid-driven cavity geometry using up to 5 million Chebyshev collocation nodes and an efficient decoupling of velocity and pressure computations, which permitted following the flow through transition into turbulence in the range $12\,000 \leqslant Re \leqslant 22\,000$.

As far as global instability analysis of three-dimensional (cubical) cavities is concerned, substantially less work has been performed, no doubt owing to the challenging nature of the related eigenvalue problem solutions. The first solution of the pertinent three-dimensional eigenvalue problem has been presented recently by Giannetti, Luchini & Marino (2009). Essential for the success of the computations has been an approximate inversion technique incorporated in the algorithm developed by these authors, which permitted high-resolution global instability analyses. Results obtained on a 128^3 spectral collocation grid revealed the structure of the leading three-dimensional global eigenmode at $Re = 2000$. Independently, Feldman & Gelfgat (2010) also analysed three-dimensional flow instability in this flow and identified the leading mode of the cubic cavity to be associated with a Hopf bifurcation at $Re \approx 1900$. Three-dimensional global instability analysis of spanwise inhomogeneous three-dimensional lid-driven cavity flows represents one of the latest research frontiers in this class of flows.

Turning away from regular rectangular domains, a number of theoretical predictions of flow exist in (two-dimensional) cavities of complex two-dimensional profiles. Ribbens *et al.* (1991) described the flow in an elliptic region with a moving boundary, while Darr & Vanka (1991) have studied two-dimensional flow in a trapezoidal cavity, permitting lid motion of either of the unequal trapezium sides and documenting the respective steady flow patterns in the Reynolds number range $Re \in [100, 1000]$. Motivated by the aforementioned prediction of Batchelor (1956), the same trapezoidal lid-driven cavity flow, as well as flow in an equilateral triangular cavity, was solved by McQuain *et al.* (1994) in the range $Re \in [1, 500]$, while Ribbens, Watson & Wang (1994) addressed the equilateral triangular lid-driven cavity flow in the same Reynolds number range. Several lid-driven cavity geometries of complex two-dimensional cross-sectional profile may be built by superposition of rectangular domains. The two most representative cases discussed in the literature as demonstrators of algorithms for the numerical solution of the equations of motion in complex geometries are the *L-shaped cavity*, introduced by Perng & Street (1991) and further studied by Oosterlee *et al.* (1993), and the *two-box-cavity* proposed by Hinatsu & Ferziger (1991), which is still the subject of intense research (e.g. Zhou *et al.* 2003; Nithiarasu & Liu 2005; Ahusborde & Glockner 2010). One of the investigation's closest related with the present work is the analysis of lid-driven cavity flow in a two-dimensional domain of quarter–circular cross-section by Vynnycky & Kimura (1994), who reported steady flow patterns in $Re \in [0, 1000]$. These authors derived an analytical solution to the steady flow problem, valid up to $Re \approx 10$, and reported numerical predictions at the higher Reynolds numbers considered in their analysis. Most of the issues encountered in the last two works, related with the singularities in the boundary conditions at the moving-lid endpoints, were overcome by Jyotsna & Vanka (1995) and later by Gaskell,

Thompson & Savage (1999), who made use of triangular grids in which corners do not require special treatment. In more recent times, Erturk & Gokcol (2007) have revisited the triangular lid-driven cavity flow in two spatial dimensions and demonstrated that the analytical predictions of Batchelor (1956) are less successful in this geometry in the high-Reynolds-number limit, as compared with the rectangular domains.

However interesting the issue of high-Reynolds-number numerical solutions of lid-driven cavity flows in such geometries may be, the possibility needs to be examined in each complex cross-sectional geometry that the corresponding steady two-dimensional flow becomes three-dimensionally unstable. Three-dimensional (BiGlobal) instability of lid-driven cavity of equilateral triangular shape was analysed by González, Theofilis & Gómez-Blanco (2007), who used a standard Taylor–Hood finite-element method on unstructured grids and the Arnoldi algorithm for the recovery of the leading part of the eigenspectrum to predict a critical Reynolds number for three-dimensional instability at ($Re_c \approx 1870, k_c \approx 6.73$). BiGlobal instability of the L-shaped cavity has been addressed by de Vicente, Theofilis & Valero (2010*b*), who identified the critical conditions of this flow as ($Re_c \approx 650, k_c \approx 9.7$). Finally, the two-box-cavity has been analysed by de Vicente *et al.* (2010*a*) with respect to its three-dimensional instability, as has been a symmetrized, cross-shaped version of the same obtaining ($Re_c \approx 170, k_c \approx 2.42$) for the first and ($Re_c \approx 605, k_c \approx 3.25$) for the second geometry.

In the present contribution, we return to two lid-driven cavity flow configurations developing in a three-dimensional container having an isosceles triangular cross-sectional profile with a right angle between the equal sides and a homogeneous third spatial direction. The flow is driven by the motion of one of the equal sides either towards or away from the right angle. Theoretical and experimental investigations have been performed in order to establish stability boundaries. In § 2, the geometry, the experimental setup and the numerical models are presented, while § 3 discusses results of basic flow calculations and the subsequent theoretical analysis; the latter results are compared with those of the associated experimental investigation. Finally, in § 4, conclusions derived from the present work are discussed.

2. Formulation of the problem and methods of investigation

2.1. *Geometry*

We consider the incompressible flow in a cavity with a triangular cross-section in which two equal sides enclose a rectangular corner. One of the sides serves as a rigid lid which moves with constant velocity either away or towards the rectangular corner and in the plane defining the triangle. The geometry and the coordinate system are shown in figure 1. The geometry and the rigid boundary conditions allow for a steady two-dimensional flow in the (x, y)-plane. We are interested in the spontaneous symmetry breaking of this steady two-dimensional flow.

2.2. *Experimental*

Experiments have been performed using a modified version of the two-sided lid-driven-cavity apparatus of Siegmann-Hegerfeld *et al.* (2008). The apparatus consists of two rotating cylinders mounted horizontally and parallel in a container which is filled with the working fluid such that the cylinders are fully immersed in the liquid (figure 2). A cavity is formed in the narrow gap between the two cylinders by mounting a horizontal bottom and a transparent lid. The cavity is closed in z-direction by transparent end plates (not shown) which are machined to fit the radius of curvature of the cylinders. The resulting approximately rectangular cavity

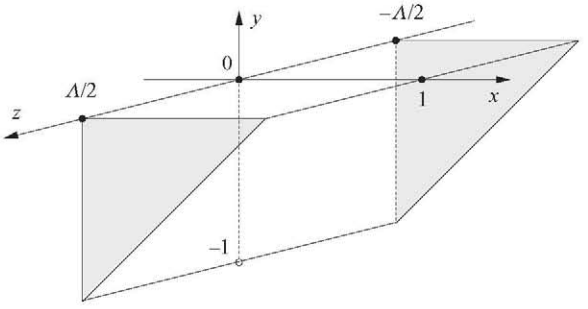

FIGURE 1. Perspective representation of the geometry of the triangular cavity using dimensionless variables. The volume is bounded by a wall at $x=0$, $y=0$ and $y=x-1$. The wall (lid) at $y=0$ moves parallel to the x-axis.

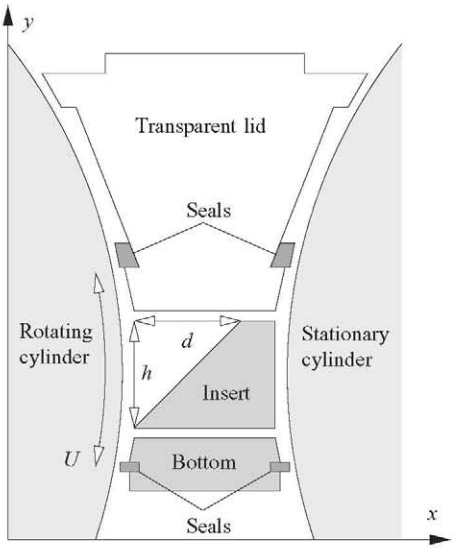

FIGURE 2. Cross-section of the (x, y)-plane of the experimental set-up. The transparent lid, insert and bottom are machined to fit the radius of the rotating and the stationary cylinder leaving a small gap of less than 0.05 mm. The seals minimize the residual through flow. The gaps between individual parts are exaggerated for clarity of representation.

is bounded by plane walls except for two lateral walls which are made by the two rotating cylinders. Their radii ($R=135\pm0.03$ mm) are much larger than the height h of the cavity. To adapt the apparatus for the present purpose, an insert has been machined such that an approximately triangular cavity is formed within the larger nearly rectangular cavity. The height h and width d of the rectangular cavity were $d=h=40$ mm. The spanwise length of $l=434$ mm yields a spanwise aspect ratio of $\Lambda=10.85$. For the present experiment, the idle cylinder was kept at rest while the other one was rotating with constant angular velocity.

The working fluid was Baysilone M20 silicone oil (Bayer) with a nominal kinematic viscosity of $\nu=22.2$ mm^2 s^{-1} at $T=20\,^{\circ}$C. We used, however, a gauge curve for $\nu(T)$ which was measured separately before the experiments. The cylinders are driven via gear belts by two computer-controlled DC servo motors. The rotation rate of the cylinder was periodically updated to account for temperature-induced changes of

$\nu(T)$ such as to keep the Reynolds number constant. The temperature was measured by two thermo-elements PT1000. The forced convection in the cavity as well as in the outer containment (the total volume of silicone oil was about 62 l) guaranteed a homogeneous temperature distribution.

Visualization was accomplished by small amounts (up to 0.013 weight percent) of aluminium flakes added to the liquid. For laser Doppler velocimetry, we used a fibre-Flow 2D-LDA System of DANTEC Dynamics and small particles (Potters Spherical 110P8CP00) with density $\rho = 1.1\ \mathrm{g\,cm^{-3}}$. The concentration was 5.6×10^{-4} weight percent. For the laser Doppler measurements, the measurement head was traversed above the triangular cavity.

2.3. *Numerical*

We consider the motion of an incompressible Newtonian fluid with density ρ and kinematic viscosity ν. The motion is governed by the Navier–Stokes and continuity equations

$$\frac{\partial \boldsymbol{u}}{\partial t} + \boldsymbol{u}\cdot\nabla\boldsymbol{u} = -\nabla p + \frac{1}{Re}\nabla^2\boldsymbol{u}, \tag{2.1a}$$

$$\nabla\cdot\boldsymbol{u} = 0. \tag{2.1b}$$

Here, we have used the scales d, d/U, U and ρU^2 for lengths, time, velocity and pressure, respectively, where d is the cavity width and U the velocity of the lid. In this particular geometry, the cavity height h has the same length as the cavity width d (unit aspect ratio $\Gamma = h/d = 1$). The Reynolds number is defined as

$$Re = \frac{|U|d}{\nu}. \tag{2.2}$$

The equations must be solved in the triangular domain Ω bounded by $\partial\Omega$.

2.3.1. *Steady laminar basic flows*

The problem allows for a steady two-dimensional basic state $(\boldsymbol{u}_0, p_0)^{\mathrm{T}}(\boldsymbol{x}) \equiv (u_0, v_0, 0, p_0)^{\mathrm{T}}(x, y)$ with $w_0 \equiv 0$, $\partial/\partial t = 0$. It must satisfy the basic-state equations

$$\boldsymbol{u}_0\cdot\nabla\boldsymbol{u}_0 = -\nabla p_0 + \frac{1}{Re}\nabla^2\boldsymbol{u}_0, \tag{2.3a}$$

$$\nabla\cdot\boldsymbol{u}_0 = 0, \tag{2.3b}$$

subject to the boundary conditions $u_0 = v_0 = 0$ on the stationary walls. The flow is driven by the motion of the lid at $y = 0$ which moves steadily either in the positive or the negative x-direction

$$\boldsymbol{u}_0(y = 0) = U\boldsymbol{e}_x, \tag{2.4}$$

where $\boldsymbol{e}_x$ is the unit vector in x-direction. On all other walls, no-slip conditions $\boldsymbol{u}_0 = 0$ hold.

The basic equations are solved by two independent methods. One method is Newton–Raphson iteration which is known for its rapid (quadratic) convergence. Alternatively, we compute the basic flow by time integration of (2.3), supplemented by a temporal (τ) derivative term, using the semi-Lagrangian finite-element solver ADFC (González & Bermejo 2005). The integration was started from a state of rest $[(\boldsymbol{u}_0, p_0)(\tau = 0) = 0]$ and terminated when the criterion

$$\max_j\{|g_j(\tau + \Delta\tau) - g_j(\tau)|\} < 10^{-15} \tag{2.5}$$

was satisfied, g_j being the local value of any flow quantity at any node j and $\Delta\tau$ the step size for the time integration.

The mathematical problem is singular as the velocity boundary conditions are discontinuous on both ends of the moving lid. To clarify the effect of the numerical regularization of the exact boundary conditions on the global flow and its stability, we numerically employed (2.4) as well as the strongly regularized boundary condition

$$\boldsymbol{u}_0(x, y = 0) = U\boldsymbol{e}_x \left[1 - (2x - 1)^{18}\right]^2, \tag{2.6}$$

in which the lid velocity is filtered as in Leriche, Gavrilakis & Deville (1998) as an alternative to (2.4). We note that a numerical implementation of (2.4) likewise represents a regularization, albeit on the very small scale of the grid size. Keeping this in mind, we shall refer, henceforth, to the 'singular problem' when using (2.4) and to the 'regularized problem' when using (2.6).

2.3.2. *Linear stability: eigenvalue problem formulation and solution methodology*

Since we are interested in the linear stability of the two-dimensional steady basic flow, we consider perturbations $(\tilde{\boldsymbol{u}}, \tilde{p})$ such that the total flow fields are

$$\boldsymbol{u} = \boldsymbol{u}_0 + \tilde{\boldsymbol{u}}, \tag{2.7a}$$

$$p = p_0 + \tilde{p}. \tag{2.7b}$$

Substituting (2.7) into (2.1) and linearizing with respect to $\tilde{\boldsymbol{u}}$, the perturbation equations

$$\frac{\partial \tilde{\boldsymbol{u}}}{\partial t} + \boldsymbol{u}_0 \cdot \nabla\tilde{\boldsymbol{u}} + \tilde{\boldsymbol{u}} \cdot \nabla\boldsymbol{u}_0 = -\nabla\tilde{p} + \frac{1}{Re}\nabla^2\tilde{\boldsymbol{u}}, \tag{2.8a}$$

$$\nabla \cdot \tilde{\boldsymbol{u}} = 0, \tag{2.8b}$$

are obtained. The perturbation flow must satisfy the no-slip boundary conditions $\tilde{\boldsymbol{u}} = 0$ on $\partial\Omega$. Since the coefficients of (2.8) do not depend on z and t, the perturbation quantities can be written as normal modes

$$\tilde{\boldsymbol{u}} = \hat{\boldsymbol{u}}(x, y)\, \mathrm{e}^{\gamma t + \mathrm{i}kz} + \text{c.c.}, \tag{2.9a}$$

$$\tilde{p} = \hat{p}(x, y)\, \mathrm{e}^{\gamma t + \mathrm{i}kz} + \text{c.c.}, \tag{2.9b}$$

where the complex conjugate (c.c.) is required to render the perturbations real. Here, we are interested in the temporal stability analysis in which the wavenumber $k \in \mathbb{R}$ is assumed to be real while $\gamma = \sigma + \mathrm{i}\omega \in \mathbb{C}$ is the complex growth rate with real growth rate σ and oscillation frequency ω.

Substitution of the ansatz (2.9) into the perturbation equations (2.8) yields

$$\left(\mathscr{L} + \frac{\partial u_0}{\partial x}\right)\hat{u} + \hat{v}\frac{\partial u_0}{\partial y} + \frac{\partial \hat{p}}{\partial x} = -\gamma\hat{u}, \tag{2.10a}$$

$$\left(\mathscr{L} + \frac{\partial v_0}{\partial x}\right)\hat{v} + \hat{u}\frac{\partial v_0}{\partial x} + \frac{\partial \hat{p}}{\partial y} = -\gamma\hat{v}, \tag{2.10b}$$

$$\mathscr{L}\hat{w} + \mathrm{i}k\hat{p} = -\gamma\hat{w}, \tag{2.10c}$$

$$\frac{\partial \hat{u}}{\partial x} + \frac{\partial \hat{v}}{\partial y} + \mathrm{i}k\hat{w} = 0, \tag{2.10d}$$

where $\mathscr{L}$ is the linear advection–diffusion operator

$$\mathscr{L} = u_0\frac{\partial}{\partial x} + v_0\frac{\partial}{\partial y} - \frac{1}{Re}\left(\frac{\partial^2}{\partial x^2} + \frac{\partial^2}{\partial y^2} - k^2\right). \tag{2.11}$$

For the present case of a basic flow velocity vector $(u_0, v_0, 0)^{\mathrm{T}}$ normal to the wave vector $k\boldsymbol{e}_z$, it is possible to deduce a real eigenvalue problem (thus halving the memory requirements for its solution) by re-defining the out-of-plane velocity component (Theofilis 2003)

$$\hat{w} \rightarrow -\mathrm{i}\hat{w}. \tag{2.12}$$

This converts the system (2.10) into the real generalized eigenvalue problem

$$A \cdot \boldsymbol{X} = -\gamma B \cdot \boldsymbol{X}, \tag{2.13}$$

where $\boldsymbol{X} = (\hat{u}, \hat{v}, \hat{w}, \hat{p})^{\mathrm{T}}$ and the linear operators A and B are real. The eigenvalues γ of such a real eigenvalue problem are either real or they arise as pairs of complex conjugate eigenvalues. The corresponding eigenvectors describe, for vanishing growth rate $\sigma = 0$, either stationary modes ($\gamma = 0$) or travelling waves ($\gamma = \pm \mathrm{i}\omega \neq 0$), respectively.

To discretize the equations, we use a triangular-element-based unstructured mesh, since it is ideally suited for the triangular geometry; further details as well as the entries of all matrices are presented in the Appendix of González *et al.* (2007). An unstructured mesh of uniform-sized equilateral triangular elements having a side of size 0.01 has been used. The eigenvalue problem is solved using a Krylov-subspace iteration, originally proposed by Saad (1980) and discussed in detail by Theofilis (2003). Computations have been performed serially on a PC, using typical leading dimension of the matrix A of $\mathrm{DIM}(A) \equiv 3N_u + N_p = O(7 \times 10^4)$, where N_u and N_p are the numbers of quadratic velocity- and linear pressure-nodes, respectively. Sparse linear algebra algorithms have been used in order to obtain the LU decomposition necessary within the Arnoldi method, which permits storing only the $O(9 \times 10^6)$ non-zero elements of this matrix. The total time needed for a complete Arnoldi analysis depends on the one hand on the efficiency of this linear solver, and on the other hand on the Krylov space dimension m used to approximate the leading eigenvalues. In this case, the size of the Krylov space dimension used and consequently the number of eigenvalues computed by the Arnoldi algorithm is $m = 100$. We should also remark that no shift parameter has been used for these calculations.

3. Results

3.1. *Basic flows*

Basic flows in triangular cavities using the singular boundary conditions (2.4) have been discussed extensively by Erturk & Gokcol (2007) and references cited therein (Ribbens *et al.* 1994; Jyotsna & Vanka 1995; Li & Tang 1996; Gaskell *et al.* 1999). Here, we provide results for the right-angled-triangular geometry, the vertices of which are chosen at the points $(x, y) = (0, 0)$, $(1, 0)$ and $(0, -1)$, as shown in figure 1. These steady two-dimensional flows having the same symmetries as the boundary conditions are stable at sufficiently small Reynolds numbers. This is confirmed by experiments in long cavities in which quasi-two-dimensional cavity flows are observed.

3.1.1. *Motion away from the rectangular corner*

Figure 3 shows visualizations of the basic state streaklines in a vertical cut at $z = 0$ for two subcritical Reynolds numbers and lid motion away from the 90° and towards the 45° corner. One can distinguish the primary vortex for low Reynolds numbers (–200). Also, for $Re \gtrsim 250$, a secondary and a tertiary vortex can be identified in the experiments. As the Reynolds number increases, the region of flow separation grows

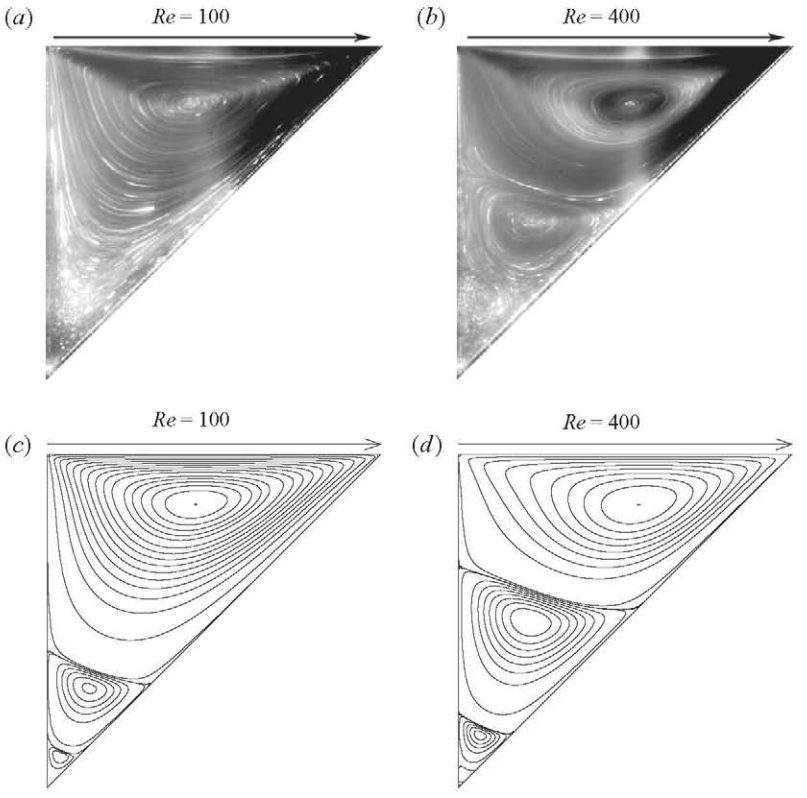

FIGURE 3. Wall motion away from the rectangular corner. The lid moves rightwards as indicated by the arrow. The photographs show streak lines in the (x, y)-plane at $z=0$ for $Re=100$ (a) and $Re=400$ (b) (subcritical conditions). The exposure time was 2 s at $f=1:27$. The numerically computed contours of the stream function are shown in (c,d). In (c), 20 equidistant levels in each of the ranges $[-6.2\times10^{-2}, -1.0\times10^{-4}]$ and $[0, 6.2\times10^{-5}]$ and 10 equidistant levels in $[-3.75\times10^{-8}, 8.8\times10^{-8}]$ are shown. In (d), 20 equidistant levels were used in each of the ranges $[-5.8\times10^{-2}, -2.0\times10^{-3}]$, $[0, 1.4\times10^{-3}]$ and $[-8\times10^{-7}, 2.2\times10^{-6}]$ and 10 equidistant levels within $[-2.2\times10^{-10}, 2.2\times10^{-10}]$.

in size and the centre of the primary vortex is shifted downstream the moving wall, a typical effect of inertia.

3.1.2. *Motion towards the rectangular corner*

Figure 4 shows visualizations of the basic state streaklines in a vertical cut at $z=-1$ for different Reynolds numbers and lid motion towards the rectangular corner. A secondary vortex is clearly visible even for $Re=100$. The tertiary vortex is less evident than that for the wall motion away from the 90° corner. The location of the centre of the primary vortex changes slightly in the vertical direction with the Re number. In the experiments, we observe for $Re \gtrsim 350$ a weak flow separation on the stationary diagonal wall where the fluid is sucked into the upstream corner of the moving wall. This separation did not occur in the numerical solution, but the near-wall flow is significantly slowed down in this region.

3.1.3. *Basic flow: numerical results*

Numerical results for the basic state were obtained typically for $N_u=23\,232$ (quadratic) velocity nodes and $N_p=5894$ (linear) pressure nodes. The data obtained

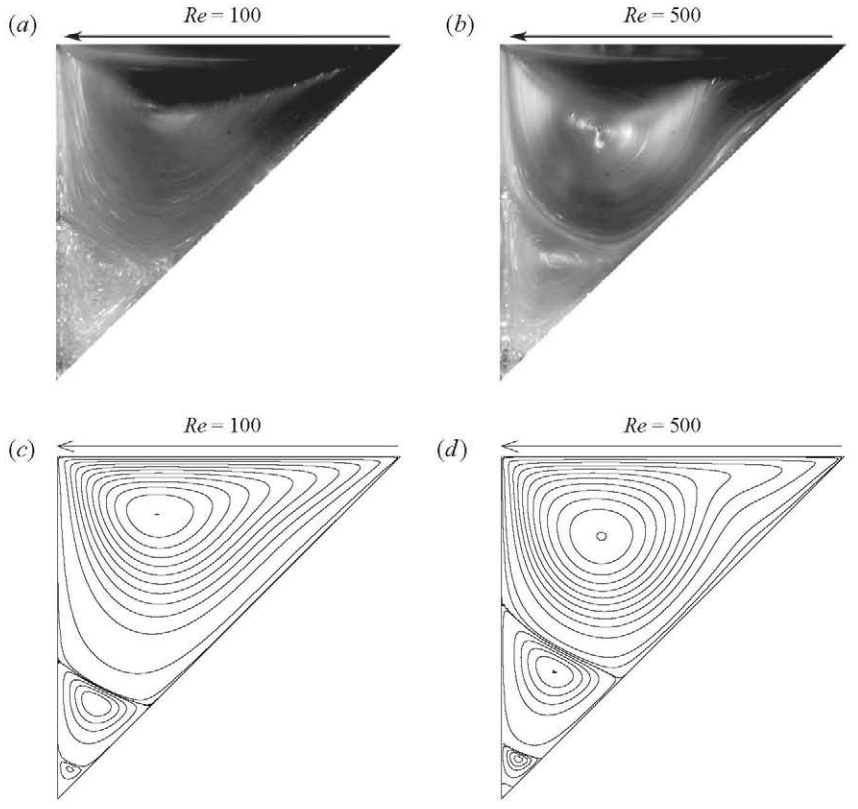

FIGURE 4. Wall motion towards the rectangular corner. The wall motion is indicated by the arrow. The photographs show streak lines in the (x, y)-plane at $z = -1$ for $Re = 100$ (a) and $Re = 500$ (b) (subcritical conditions). The exposure time was 2 s at $f = 1 : 27$. The numerically computed contours of the stream function are shown in (c,d). In (c), 20 equidistant isolines were used for each of the intervals $[10^{-5}, 0.07]$ and $[-7.15 \times 10^{-5}, 0]$ and 10 equidistant isolines within $[-10^{-8}, 4.3 \times 10^{-8}]$. In (d), we used 20 isolines in $[-0.058, -0.002]$, $[10^{-5}, 0.077]$ and $[-1.4 \times 10^{-3}, 0]$ and 10 isolines in $[-10^{-7}, 9 \times 10^{-7}]$.

have been confirmed by higher resolution computations as shown in tables 1 and 2, where results of grid convergence studies are summarized. The tabulated data have been obtained using a homogeneous mesh when using Newton's method and, alternatively, a nearly homogeneous mesh using a commercial mesh generator in case of the time marching method. As the grids used for the two methods are different with different distribution of the nodal points in space, the position of the maxima and minima for the nodal variable corresponds to different locations as can be seen from columns for space locations in the two tables. Still, the maximum difference for the fine meshes is about 2.25 % which occurs for the maximum of the v_0 in table 1. Note that our meshes are substantially finer than those used by Ding & Kawahara (1998), who also used a finite-element method to solve the related problem of the (singular) lid-driven square-cavity problem.

For basic state calculations by time-stepping, we used the time-step $\Delta t = 0.01$. This value yields moderate total run times. As an example, we show in figure 5, the basic velocity components along line $x = -y$ for both methods employed. It can be seen that the results of both the methods are in excellent agreement.

Nodes	$\min u_0$	$x^{\min u_0}$	$y^{\min u_0}$	$\max v_0$	$x^{\max v_0}$	$y^{\max v_0}$	$\min v_0$	$x^{\min v_0}$	$y^{\min v_0}$
				Time marching					
9236	−0.43857	0.64556	−0.21948	0.18302	0.39923	−0.19964	−0.38044	0.81006	−0.12990
15 485	−0.44045	0.65872	−0.22355	0.19044	0.38945	−0.19263	−0.38586	0.80699	−0.13105
28 525	−0.44414	0.66383	−0.22957	0.19124	0.38320	−0.18828	−0.38731	0.80065	−0.13910
36 103	−0.44513	0.67157	−0.22554	0.19152	0.37638	−0.18043	−0.38868	0.79731	−0.14390
				Newton–Raphson					
9180	−0.45069	0.67910	−0.22388	0.19575	0.38059	−0.17910	−0.39412	0.79850	−0.14179
15 400	−0.45072	0.67816	−0.22413	0.19577	0.37931	−0.18390	−0.39437	0.79885	−0.14367
23 220	−0.45074	0.67757	−0.22429	0.19586	0.37850	−0.18224	−0.39419	0.80373	−0.14018
36 315	−0.45072	0.67164	−0.22761	0.19584	0.37687	−0.17911	−0.39425	0.79478	−0.14552

TABLE 1. Extrema of the basic velocity field for $Re = 560$ and the respective (x, y)-coordinates as functions of the number of nodes used for the regularized case when the lid moves in positive x-direction.

Nodes	$\min u_0$	$x^{\min u_0}$	$y^{\min u_0}$	$\max v_0$	$x^{\max v_0}$	$y^{\max v_0}$	$\min v_0$	$x^{\min v_0}$	$y^{\min v_0}$
				Time marching					
9236	0.38956	0.25784	−0.44745	0.35845	0.52054	−0.27934	−0.63896	0.03944	−0.12753
15 485	0.39340	0.26328	−0.45034	0.35692	0.51789	−0.28393	−0.64386	0.03583	−0.13274
28 525	0.39782	0.26756	−0.45109	0.35517	0.51603	−0.28649	−0.64582	0.03479	−0.13872
36 103	0.39774	0.27158	−0.45284	0.35478	0.51565	−0.28838	−0.64676	0.03464	−0.14000
				Newton–Raphson					
9180	0.40336	0.268657	−0.455224	0.36122	0.514925	−0.291045	−0.65691	0.037313	−0.149254
15 400	0.40337	0.270115	−0.454023	0.36128	0.517241	−0.287356	−0.65776	0.034483	−0.137931
23 220	0.40334	0.271028	−0.453271	0.36123	0.518692	−0.285047	−0.65677	0.032710	−0.130841
36315	0.40328	0.272388	−0.455224	0.36122	0.518657	−0.287313	−0.65726	0.033582	−0.138060

TABLE 2. Extrema of the basic velocity field for $Re = 780$ and the respective (x, y)-coordinates as functions of the number of nodes used for the regularized case when the lid moves in the negative x-direction.

As can be seen from figures 3 and 4, the numerically computed streamlines agree satisfactorily with the experimental results. The major difference is the absence of secondary vortices in the experiment when the lid moves slowly away from the rectangular corner (figure 3*a*). For higher Reynolds numbers, the secondary eddies are visible both in the experiment and in the numerical solution. This behaviour might be related to an endwall effect which is expected to create a weak secondary flow also in the plane $z = 0$ which is visualized in figure 3(*a*). The suppression of the secondary vortices for slow flow is not observed in the case when the lid moves towards the rectangular corner. In the latter case, the visualization plane was selected slightly off-centre at $z = -1$.

3.2. *Linear stability analysis and supercritical flow structures for the motion away from the rectangular corner*

3.2.1. *Experimental observations*

To visualize the flow patterns, aluminium flakes have been added to the silicone oil. Depending on the local flow properties (flow direction and rotation rate), there exists a preferred mean orientation of the flakes. When the liquid is illuminated by a suitable

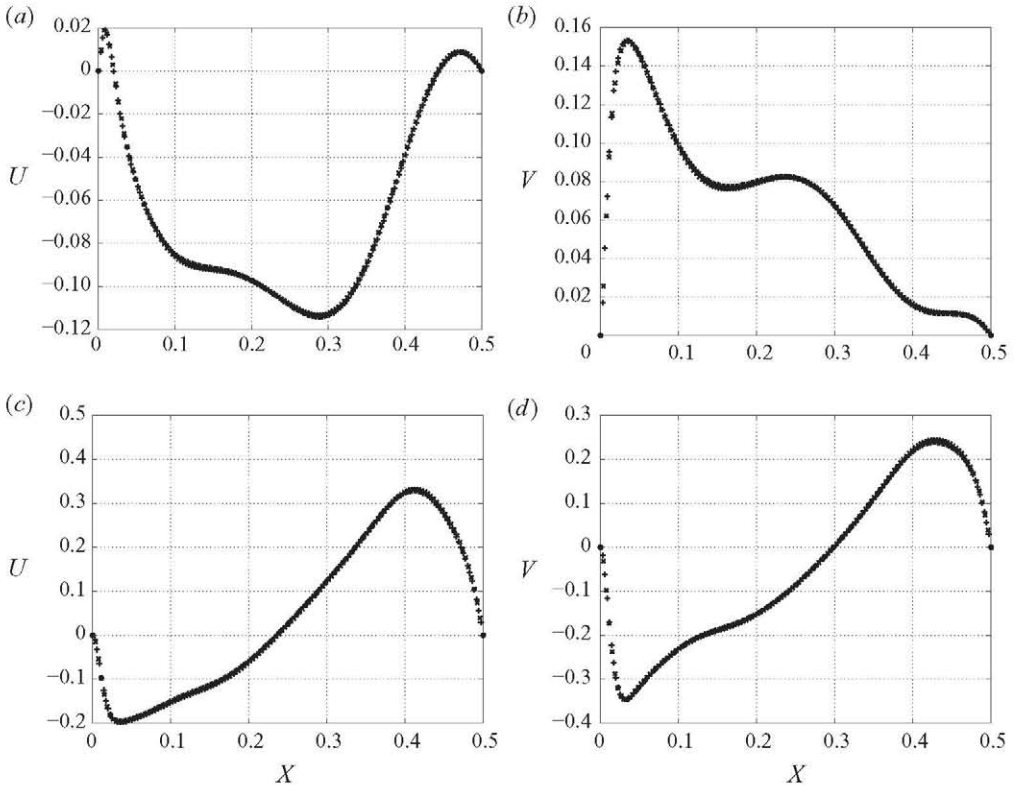

FIGURE 5. Basic velocity values along the line $x = -y$ for $Re = 560$ (top figures) and the lid moving in the positive x-direction and $Re = 780$ and the lid moving in the negative x-direction (bottom figures). In both cases, regularized boundary conditions were used. Time marching (+), Newton–Raphson (×).

light source, flow inhomogeneities become easily observable due to the difference in local reflectivity. The interpretation is difficult, since the intensity of the reflected light depends on the direction of the incident light, the direction of observation and the local flow. However, qualitative changes of the flow and its spatial period are easily detected.

The basic flow for wall motion away from the rectangular corner becomes unstable to a stationary three-dimensional flow via a supercritical bifurcation. Figure 6 shows the evolution of the stationary flow patterns in the (y, z)-plane of the full cavity for a series of increasing Reynolds numbers. Near the critical threshold, the endwall effects drive a perturbation flow whose amplitude decays from both endwalls at $z = \pm \Lambda/2$ towards the interior of the cavity. As Re increases, the primary vortex readily becomes wavy along its axis throughout the whole length. Experimentally, we can bracket the critical onset to $Re_c \in [550, 590]$.

The closeup in figure 7 illustrates the fine structure of the fully developed three-dimensional pattern. It consists of cells whose boundaries are nearly perfectly perpendicular to the z-axis and characterized by $w = 0$. Note that two such cells comprise a single wavelength. The two straight vertical lines in figure 7 indicate every second cell boundary, and hence, one wavelength. The cell boundary with $w = 0$ in the middle of the figure is not clearly visible as a result of the flow structure

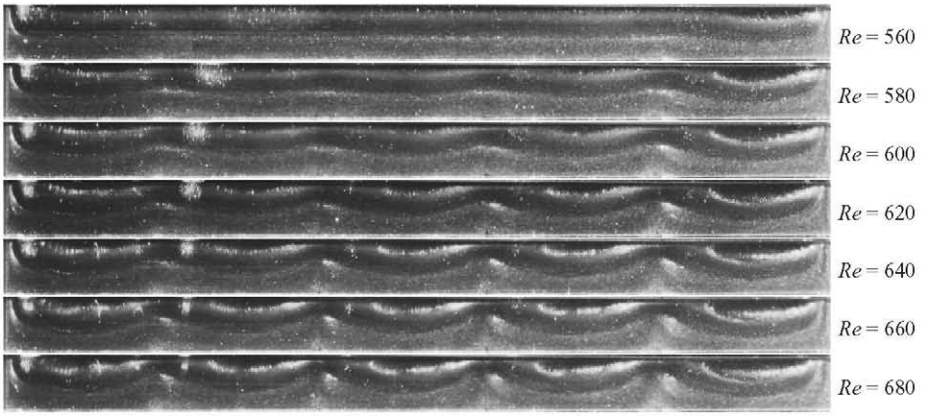

FIGURE 6. Evolution of the flow pattern in the (y, z)-plane for Reynolds numbers ranging from 560 to 680. The uncertainty in the Reynolds number is estimated to be ± 20. The laser light sheet is located at $x = 0.33$. The moving wall is located at the upper border and it moves into the plane, away from the observer.

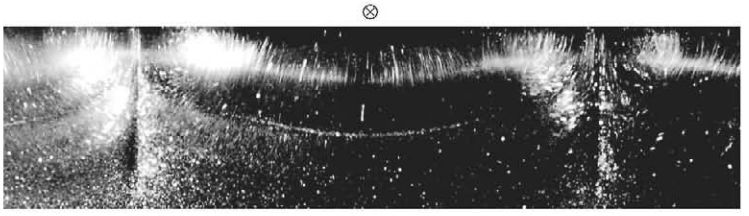

FIGURE 7. Closeup of the pattern for $Re = 700$ showing the flow over one wavelength in the middle of the cavity. The moving wall is located at the upper border and it moves into the plane, away from the observer.

and visualization technique. For all Reynolds numbers investigated, the steady three-dimensional cellular flow has a constant wavelength of $\lambda = \Lambda/5 = 2.17 \pm 4\,\%$. Of course, this wavelength must not be the most dangerous one in a infinitely extended system, because the length scales in an infinite system are not constrained by endwall effects.

To provide more detailed data on the fully developed supercritical flow, we show in figure 8 LDV measurements at $Re = 650$. The periodic structure is clearly revealed. The innermost three periods of the flow seem to be only slightly perturbed by the endwalls. Endwall effects are substantial within one wavelength of the pattern from each endwall. While the velocity component w varies nearly harmonically in the z-direction (□, lower curve in figure 8*a*), the v component contains higher harmonics in z (○, upper curve in figure 8*a*) at the measuring location. This behaviour may be expected from the strong dependence on z of the flow pattern near every second cell boundary in figure 7.

A bifurcation diagram is shown in figure 9. For the bifurcation, we measured the w component, because it should vanish for $Re < Re_c$ in the absence of finite-length effects and because it is optically accessible through the transparent wall using LDV. The measurement locations have been selected along the line $(x, y) = (0.3, -0.175)$ which provided a good signal of both the v and the w components of the perturbation flow (see figure 8). To monitor the evolution as Re increases, we fixed the z locations

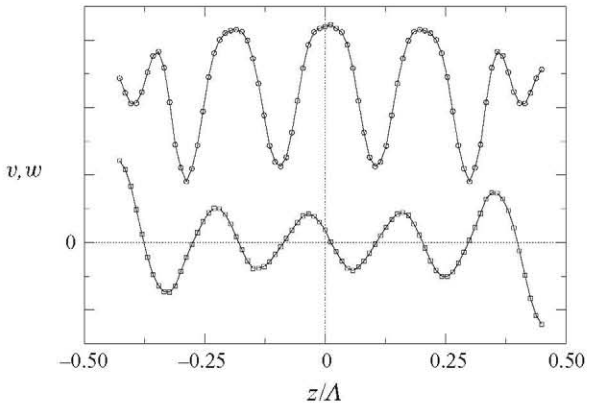

FIGURE 8. Velocity profiles in arbitrary units of $v(z)$ (○, upper curve) and $w(z)$ (□, lower curve) for $Re = 650$ taken along the line $(x, y) = (0.3, -0.175)$ which is slightly above the centre of the vortex. The spanwise aspect ratio is $\Lambda = 10.85$.

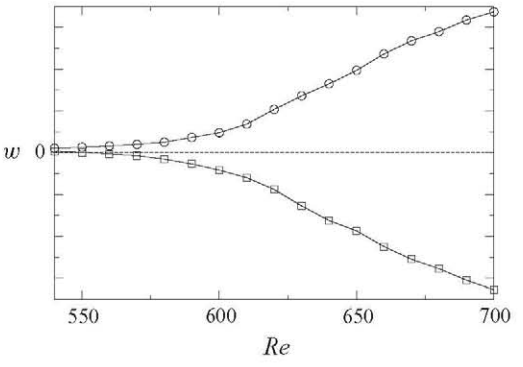

FIGURE 9. Bifurcation diagram. Shown is the velocity component w in arbitrary units as a function of the Reynolds number measured at $(x, y, z) = (0.3, -0.175, -0.375)$ (○, upper curve) and $(x, y, z) = (0.3, -0.175, 0.625)$ (□, lower curve). The full lines are guides to the eye. The velocity is given in units of mm s^{-1}.

to $z = 0.625$ and $z = -0.375$ corresponding to the two innermost local extrema of w in figure 8. The asymmetry of these locations with respect to $z = 0$ was selected to compensate the slight shift in z-direction of the pattern (figure 8) and to take measurements at the local minimum and local maximum of w near the cavity centre. As can be seen from figure 9, the measured velocities are symmetric with respect to $w = 0$. However, no clear bifurcation point can be identified. Likewise, the velocity component v (not shown) does not exhibit a clear bifurcation structure. A weakly perturbed pitchfork bifurcation is expected, since the secondary Bödewadt flow induces a velocity component w for all Re. The latter is usually very weak in a distance of a few length scales from the endwalls. In fact, the w component of the Bödewadt flow at $Re = 540$ is very small in the central part of the cavity. Unlike other instabilities, for which the endwall effect only slightly perturbs the bifurcation (see, e.g. figure 11 of Siegmann-Hegerfeld, Albensoeder & Kuhlmann 2007), the present critical mode appears to be very sensitive to the specific endwall conditions. This conclusion is supported by the observation that the perturbed basic flow close to the endwalls (e.g. figure 6 for $Re = 580$) is very similar to the fully developed flow near the

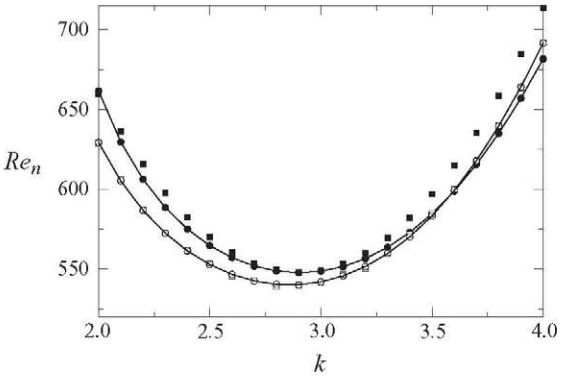

FIGURE 10. Neutral stability curve for the lid motion away from the rectangular corner using regularized boundary conditions (full symbols) and singular boundary conditions (open symbols). Results are shown for basic states obtained by the Newton–Raphson method (circles and lines) and by time marching (boxes).

cell boundaries in the middle of the cavity (e.g. figure 6 for $Re = 680$). The stationary instability mode in rectangular cavities for an aspect ratio $d/h > 1.207$ (Albensoeder *et al.* 2001*b*) which seems to be strongly related to the present unstable mode is suffering from a similar strongly imperfect bifurcation (T. Siegmann-Hegerfeld 2009).

3.2.2. *Numerical linear stability results*

Figure 10 shows the neutral stability curves for the stationary instability obtained from the two methods employed for the basic state and the two different boundary conditions: singular and regularized. For singular boundary conditions, both basic state methods yield nearly identical results. For the regularized boundary conditions, there remains a small difference between both methods which tends to vanish as the time marching is extended. The critical Reynolds and wavenumbers $Re_c = 540.2$ and $k_c = 2.86$ obtained for singular boundary conditions agree very closely with the ones for the regularized problem, $Re_c = 547.7$ at $k_c = 2.90$. Hence, the regularization of the lid velocity has only a small effect on the critical point.

For numerical efficiency, the stability analysis has been carried out varying the wave number k in discrete steps of 0.1 with much refined step size in the immediate neighbourhood of the critical wavenumber. In order to ensure that the local minimum of the neutral curve Re_n in figure 10 is indeed the critical Reynolds number, we computed the maximum growth rate σ within the wide range $k \in [1, 40]$ for a Reynolds number fixed to $Re = 540.2$. Within this extended range of wavenumbers, all growth rates were $\sigma \leqslant 0$. As an example, we show the growth rate $\sigma(k)$ in figure 11 of the least stable mode in a region within which the most dangerous mode changes from one mode to another. From these calculations, we conclude that the local minimum of $Re_n(k)$ found indeed corresponds to the critical point and the associated eigenvector represents the critical mode.

The stationary critical mode arises as a cellular pattern which is characterized by periodic planes $z = \text{const.}$ on which the spanwise perturbation flow $w = 0$ vanishes. The critical mode in such a plane is shown in figure 12 (arrows).

It is overlaid with the stream function of basic flow (lines). The perturbation flow field is significant only in the area where the basic flow is strong, i.e. near the primary eddy. In the particular plane shown, the perturbation flow arises in the form of a vortex which is slightly shifted with respect to the primary eddy of the basic flow.

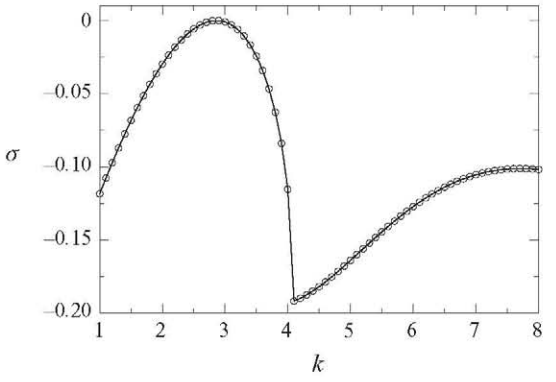

FIGURE 11. Dependence of the growth rate σ of the leading eigenmode on the wavenumber k for the lid motion away from the rectangular corner and for $Re = 540.2$ using singular boundary conditions and Newton's method for the basic state. Note that the most dangerous mode changes near $k = 4$.

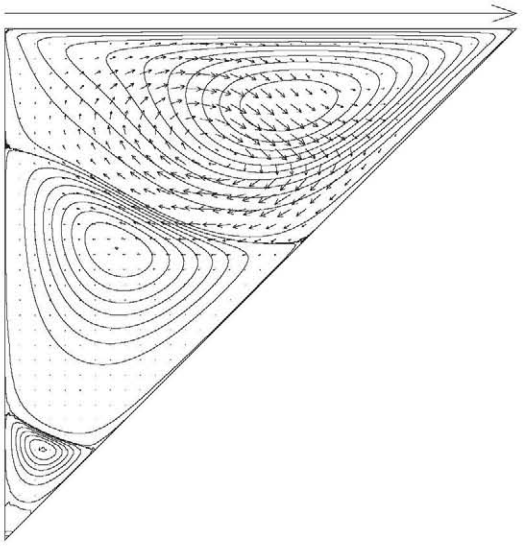

FIGURE 12. Contours of stream function of the basic flow (lines) and normalized perturbation flow field (arrows) in an (x, y)-plane $z = \text{const.}$ at the critical Reynolds number $Re_c = 540.2$ and critical wavenumber $k_c = 2.86$. The long arrow at the top of figure indicates the lid motion. The isolines are scaled differently within each vortex of the basic state.

The perturbation vortex is displaced away from the moving wall and towards the stationary side of the cavity. A superposition of the perturbation flow and the basic flow would yield a vortex in the (x, y)-plane which is slightly shifted with respect to the unperturbed primary vortex, the shift direction alternating periodically as a function of the spanwise coordinate z. To visualize the combined flow, the basic state is superposed by the suitably scaled critical mode. Views of this superposition are shown in figure 13 for two orthogonal planes at constant x and y, respectively, near the centre of the primary vortex. The cell formation is obvious from the periodic planes of constant z at which $w = 0$. This observation is in qualitative agreement with the experimental observations (figure 7). The critical wavelength $\lambda_c = 2\pi/k_c = 2.20$ is

Method	Re_c	k_c
Experimental	570 ± 20	2.89 ± 0.11
Computational singular BC	540.2	2.86
Computational regularized BC	547.7	2.90

TABLE 3. Comparison of the critical Reynolds and wavenumber values obtained when the lid moves in the positive x-direction.

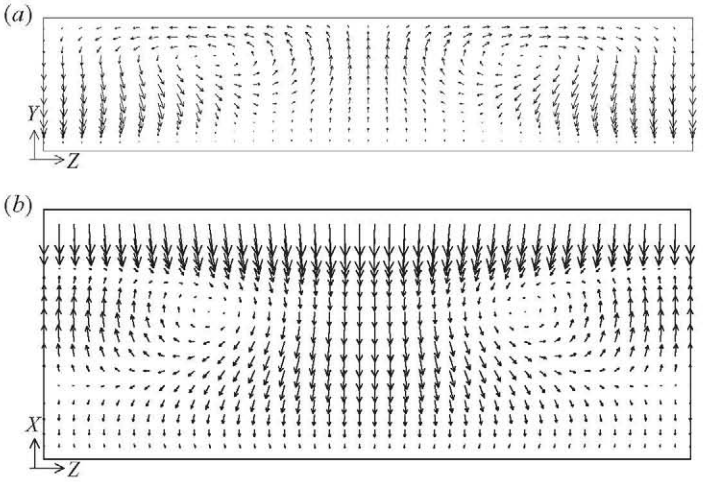

FIGURE 13. Superposition of the basic flow and the arbitrarily scaled critical mode for $Re_c = 540.2$ and $k_c = 2.86$ for one wavelength of the flow. The cross-sections shown are taken at $x = 0.55$ (a) and $y = -0.15$ (b). Both planes are close to the centre of the primary vortex.

in excellent agreement with the spatial period measured experimentally in the centre of the cavity. Also, the critical Reynolds number $Re_c = 540.2$ is in very good agreement with the lower bound on Re_c of 550 estimated from the experiment. A summary table containing the experimental values and the computational ones is shown in table 3. The slight discrepancy may be due to the fact that the three-dimensional flow cannot be measured directly on the margin of stability. Moreover, finite-length effects in the experiment cannot be completely ruled out.

3.3. *Linear stability analysis and supercritical flow structures for the motion towards the rectangular corner*

3.3.1. *Experimental observations*

The instability of the flow when the lid motion is directed towards the rectangular corner is distinctly different from the case when the lid moves in the opposite direction. In the experiments, we find a supercritical Hopf bifurcation to a three-dimensional flow. The presence of the rigid endwalls of the cavity seems to have a stabilizing effect, since for slightly supercritical conditions the amplitudes of oscillation are largest in the middle of the cavity around $z \approx 0$. We determined the critical threshold in the experiment as $Re_c = 730 \pm 20$.

Snapshots of the flow pattern are shown in figure 14. Figure 14(a) shows a modulation of the primary vortex. It is easily detectable, since tiny air bubbles accumulate in the vortex core occasionally. The vortex motion appears in the form

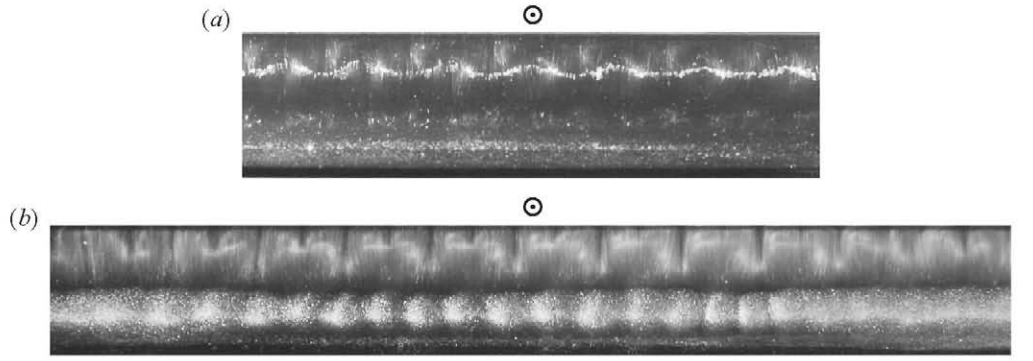

FIGURE 14. (*a*) Snapshot of the three-dimensional oscillating flow pattern for $Re = 840$ showing the central part of the cavity. (*b*) Snapshot of the flow for $Re = 950$ showing the full cavity and using an enlarged amount (10 times) of aluminium flakes. In the lower central part of the cavity also, the weak secondary vortex exhibits periodic variations. The moving wall is located at the upper border and it moves out of the plane, towards the viewer. The illumination is diffuse.

of a helical wave. In the basic subcritical flow, the two-dimensional flow exhibits a small separation bubble on the stationary diagonal wall (figure 4*b*). For supercritical conditions, it is observed that the flow periodically separates and attaches.

To better visualize the pattern, the concentration of aluminium flakes was increased by a factor of about 10. A snapshot for the larger Reynolds number $Re = 950$ is shown in figure 14(*b*). From both figures, we are able to derive the fundamental wavelength of $\lambda = 0.56 \pm 0.03$ corresponding to a wavenumber of $k = 11.2 \pm 0.6$. The oscillation period for $Re = 950$ was roughly measured to be $\omega = 11 \pm 0.5$ Hz. A sequence of snapshots is shown in figure 15.

The supercritical flow immediately above the critical onset could neither be identified by visual observation as a pure travelling nor as a pure standing wave. In order to gain more information, we measured the time dependence of $w(t)$ of a fully developed state by LDV at the point $\mathrm{M} := (x, y, z) = (0.15, -0.25, 0.25)$. Measurements were typically taken over 360 s with high burst rates. In almost all cases, the supercritical signal $w(t)$ exhibited a clear beating (not shown).

Figure 16 shows amplitude spectra A_w of w recorded at the measuring point M and for increasing values of Re slightly above the threshold. All peaks move to higher frequencies as Re is increased. The peak at about $\Omega = 11.25 = 4\Omega_n$ can safely be identified as the fourth harmonic of the angular rotation frequency Ω_n of the driving cylinder (the spectrum also contains other harmonics of Ω_n which lie beyond the limits of figure 16). At $Re = 732$, a small amplitude peak arises at $\Omega_1 = 10.56$ Hz. In convective time units of $T = d/U = d/(\Omega_n R) = 0.1062$, deduced from the fingerprint of the fourth harmonic of the cylinder's rotation rate in the spectrum, we get the experimental critical frequency of $\omega_c = \Omega_1 \times T = 1.121$.

The peak at Ω_1 indicates the oscillatory flow pattern. It quickly grows with Re and, at $Re = 735$ we find a second frequency Ω_2 slightly lower than Ω_1. On a further increase of Re, both peaks grow and, eventually, they become indistinguishable. We attribute the second amplitude peak at Ω_2 to a wave that is propagating in the opposite direction of the wave that is responsible for Ω_1. The different frequencies and amplitudes indicate that both directions of propagation are not fully equivalent. This is not surprising given the geometry imperfections of the apparatus. The amplitude of the peak at Ω_2 is smaller than the one at Ω_1. This is compatible with a slightly

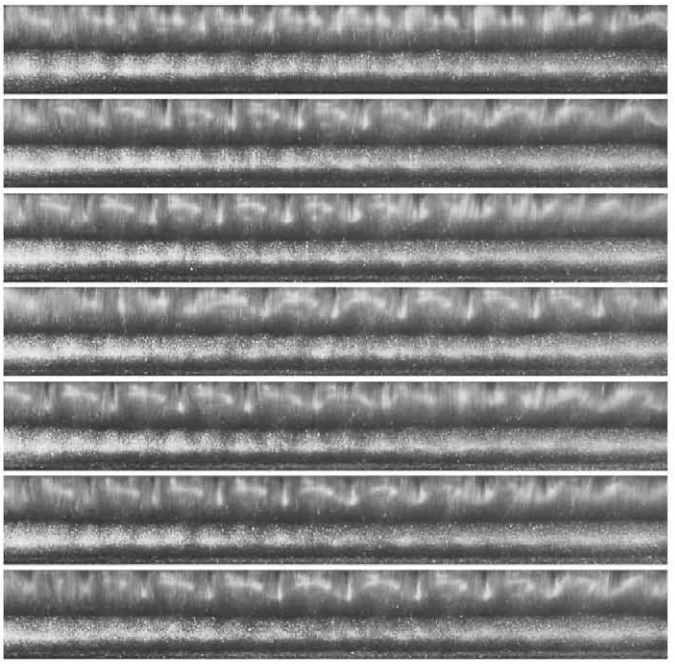

FIGURE 15. Sequence of snapshots for $Re = 850$ with a time lag of 2 s. Shown is the (x, z)-plane in diffuse light. The frames only show the central range $-4 \leqslant z \leqslant 4$. The moving wall is located at the upper border and it moves out of the plane, towards the viewer.

delayed onset of the wave corresponding to Ω_2, indicating that wave 1 is sightly favoured while wave 2 is slightly suppressed.

The linear superposition of two counter-propagating waves whose amplitudes A and frequencies Ω deviate by $2\delta \ll A$ and $2\Delta \ll \Omega$, respectively yields at leading order

$$f = (A - \delta)\sin[kx - (\Omega - \Delta)t] + (A + \delta)\sin[-kx - (\Omega + \Delta)t]$$
$$\sim A\sin(\Omega t)\cos(kx + \Delta t) + O(\delta, \Delta). \quad (3.1)$$

The nodes of the nearly standing wave would thus drift with velocity

$$c_{drift} = \frac{\Delta}{k}. \quad (3.2)$$

The drift velocity of the nodes resulting from $2\Delta = 0.03$ Hz for $Re = 735$ (figure 16*e*) is $c_{drift} = 0.11\,\mathrm{mm\,s^{-1}}$. This is in very good agreement with the visual observation. Whether the amplitude peak is split or not depends on the Reynolds number and the temporal resolution. We interpret this result as a slightly de-tuned standing wave.

3.3.2. *Numerical linear stability results*

Results of the linear stability analysis for the lid motion directed towards the rectangular corner are shown in figure 17. As before, the effect of the regularization of the lid velocity on the neutral Reynolds numbers is almost negligible. The curves have minima at $k = 10.3$ with $Re_c = 777.9$ for the singular problem and at $k = 10.3$ with $Re_c = 795.4$ for the regularized problem. The corresponding frequencies are shown in figure 18. The critical frequency for the singular problem of $\omega_c = 1.13$ is in very good agreement with the experimental frequency of $\omega_c = 1.121$. For this second

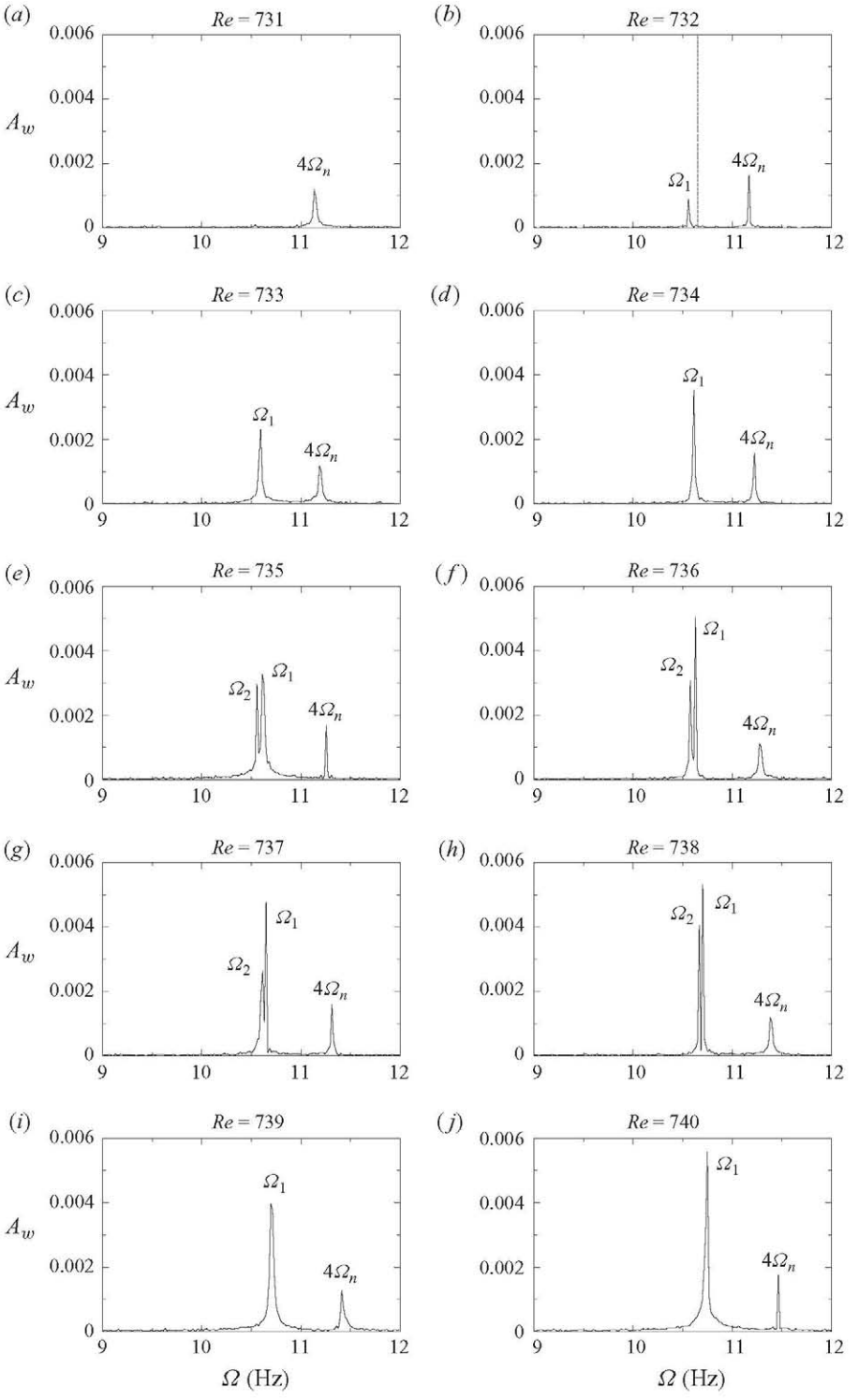

FIGURE 16. Amplitude spectrum of $w(t, 0.15, -0.25, 0.25)$ for increasing Reynolds numbers as indicated. The vertical dashed line in (b) indicates the numerical value of $\Omega_c = \omega_c/T = 10.65$.

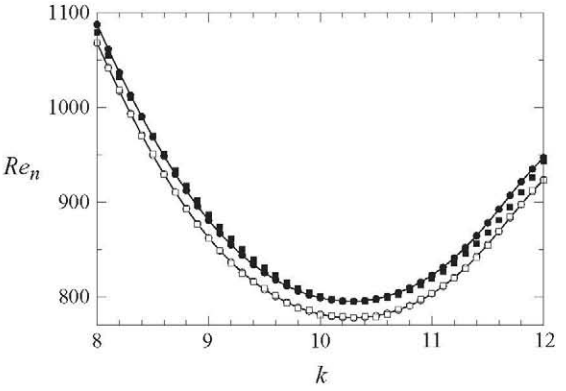

FIGURE 17. Neutral stability curve for the lid motion towards the rectangular corner using regularized (full symbols) and singular boundary conditions (open symbols). Results are shown for basic states obtained by the Newton–Raphson method (circles and lines) and by time marching (boxes).

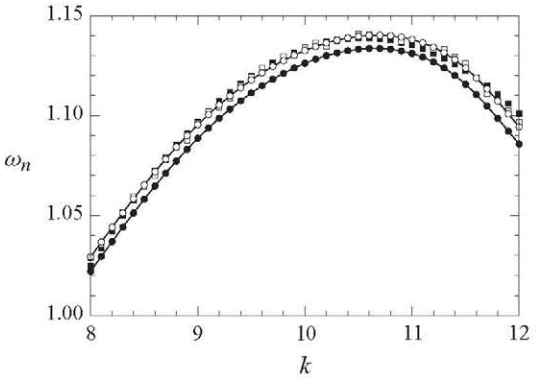

FIGURE 18. Neutral frequencies ω_n as a function of the wavenumber k of the leading eigenmode for the lid motion towards the rectangular corner using regularized (full symbols) and singular boundary conditions (open symbols). Results are shown for basic states obtained by the Newton–Raphson method (circles and lines) and by time marching (boxes).

case where the critical eigenvalues have non-zero imaginary parts, a picture showing the spectrum for the case $Re = 780$ and $k = 10.5$ is presented in figure 19.

To ensure that the local minimum of the neutral Reynolds number indeed corresponds to the critical value, the growth rate was computed for a fixed Reynolds number $Re = Re_c = 777.9$ as a function of the wavenumber in the range $k \in [1, 40]$. A close-up of the result is shown in figure 20. We did not find any positive growth rate in this wavenumber range.

In figure 21, the perturbation flow field in the (x, y)-plane in which the v-component of the perturbation flow takes its maximum absolute value at $(x_m, y_m) = (0.39, -0.36)$ (arrows) is overlaid with the stream function of the basic flow. The perturbation flow field is significant mainly in the region occupied by the primary eddy. In the plane shown, the perturbation flow arises in the form of two vortices, one below the primary eddy towards the stationary side and the other one towards the slanted wall of the cavity. A superposition of the basic flow and the scaled critical mode is shown in figure 22.

Method	Re_c	k_c	ω_c
Experimental	730 ± 20	11.2 ± 0.6	1.121 ± 0.05
Computational singular BC	777.9	10.3	1.14
Computational regularized BC	795.4	10.3	1.13

TABLE 4. Comparison of the critical Reynolds, wavenumber and frequency values obtained when the lid moves in the negative x-direction.

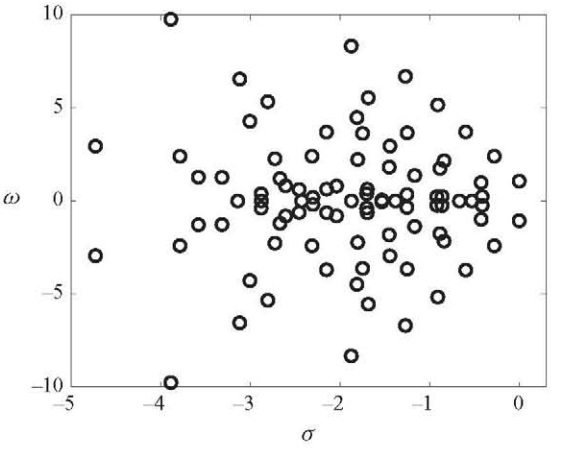

FIGURE 19. Spectrum calculated for $k = 10.5$ and $Re = 780$ for the lid motion directed towards the rectangular corner.

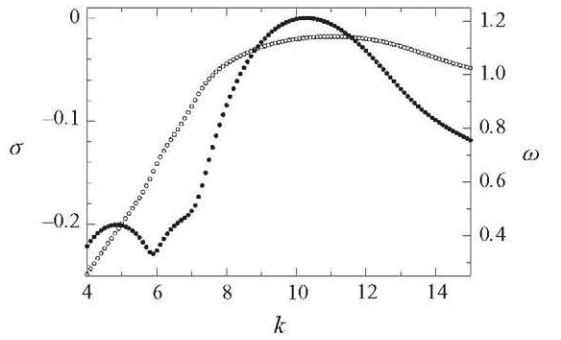

FIGURE 20. Growth rate σ (full circles) and oscillation frequency ω (open circles) of the leading eigenmode for $Re = 777.9$ obtained for singular boundary conditions and Newton's method for the basic state.

The numerical critical data $(Re_c, k_c, \omega_c)^{num} = (777.9, 10.3, 1.13)$ are in reasonably good agreement with the experimental ones $(Re_c, k_c, \omega_c)^{exp} = (732, 11.2, 1.12)$. A summary table containing the experimental values and the computational ones is shown in table 4. It is interesting to note that the structure of the critical mode for the triangular cavity with wall motion towards the rectangular corner resembles the one for shallow rectangular cavities with aspect ratio $d/h < 0.888$ as discussed by Albensoeder *et al.* (2001*b*) (their figure 8). In fact, the critical data for the rectangular cavity with an aspect ratio of $d/h = 0.5$ are $(Re_c, k_c, \omega_c) = (706, 10.6, 1.16)$

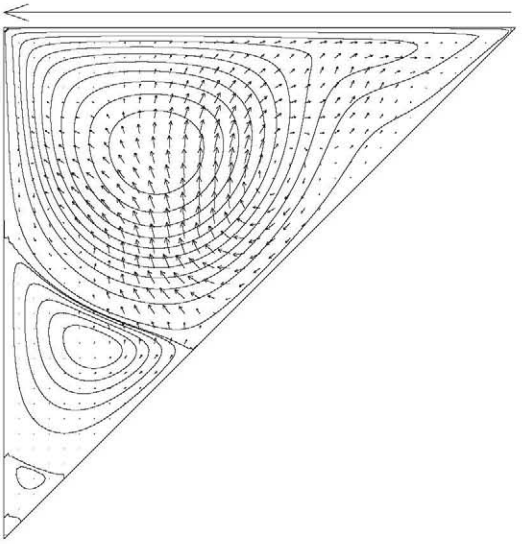

FIGURE 21. Contours of stream function (solid lines) and normalized perturbation flow field (arrows) for the critical Reynolds number $Re_c = 777.9$ and the critical wavenumber $k = 10.3$. The perturbation flow is shown in the (x, y)-plane in which the v-component of the perturbation velocity field takes its maximum absolute value. The long arrow at the top of the figure indicates the lid motion.

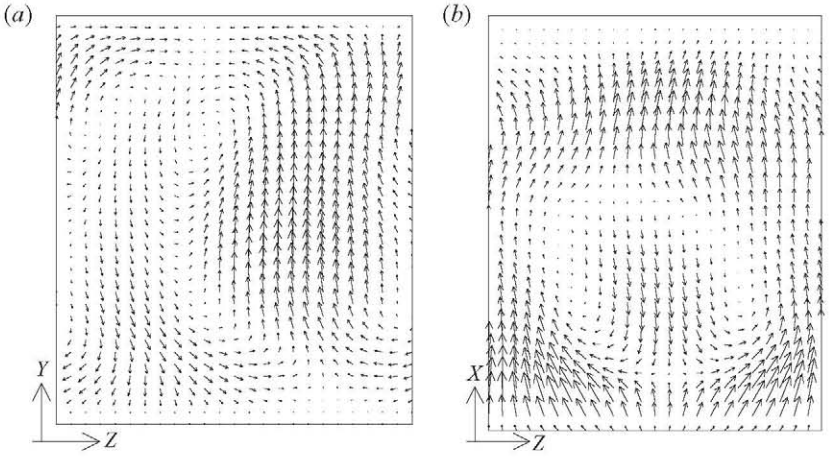

FIGURE 22. Superposition of the basic flow and the arbitrarily scaled critical mode for $Re_c = 777.9$, $k_c = 10.3$ and $\omega_c = 1.13$ for one wavelength of the flow. The cross-sections shown are taken at $x = 0.30$ (a) and $y = -0.24$ (b). Both planes are close to the centre of the primary vortex. The wave is travelling in the positive z-direction.

(Albensoeder *et al.* 2001*b*). These data are in excellent agreement with the present critical data. Also, the critical modes exhibit a very similar spatial structure.

4. Summary and conclusions

The linear stability of the incompressible flow in isosceles triangular lid-driven cavities depends on the direction of the lid motion. For lid motion away from

the rectangular corner, the critical mode is stationary. For lid motion towards the rectangular corner, the critical mode arises as a pair of three-dimensional waves propagating in two opposing spanwise directions.

The numerical results are in good to excellent agreement with experimental observations of the supercritical flow. The critical wavenumber and the visualized supercritical flow pattern of the steady mode (lid motion away from the rectangular corner) are consistent with the wavenumber and structure of the critical mode obtained from the linear stability analysis. A critical Reynolds number could not unambiguously be detected in the experiments due to strong influence of the rigid endwalls which are limiting the extension of the cavity in spanwise direction.

Regarding the oscillator instability (lid motion towards the rectangular corner), all critical parameters are in excellent agreement. The onset of the waves was accurately detected by a temporal Fourier analysis of LDV signals. The visualizations and the spectra indicate that the finite-amplitude nonlinear supercritical oscillatory flow arises in the form of a stable standing wave. The two counter-propagating waves are found to be slightly de-tuned owing to experimental imperfections.

The critical modes discovered in right-angled triangles as well as the critical parameters are very similar to the critical modes and data in the classical rectangular lid-driven-cavity problem as reported in Albensoeder *et al.* (2001*b*). The stationary mode for lid motion away from the rectangular corner has the same characteristics as the steady critical mode in deep rectangular cavity for cavity aspect ratios $\Gamma > 1.207$. For the oscillatory mode for lid motion towards the rectangular corner, we find a similarity with the oscillatory rectangular cavity mode for $\Gamma < 0.888$.

Based on the similarity of the instabilities in triangular and rectangular geometries, we conclude that the structure of the primary strained vortex is more important for the type of instability and the critical onset than the precise shape of the bounding walls. To better elucidate the universal features of the instabilities of bounded lid-driven vortices, investigations of further geometries would be of interest as well as the development of criteria which would allow an unambiguous classification of the instability mechanisms.

M. A. and H. C. K. gratefully acknowledge computing time on Phoenix provided by ZID of Vienna University of Technology. The work of V. T. has been supported by grant MICINN-TRA2009-13648: *'Metodologias computacionales para la predicción de inestabilidades globales hidrodinámicas y aeroacústicas de flujos complejos'* of the Spanish Ministry of Science and Innovation.

REFERENCES

AHUSBORDE, E. & GLOCKNER, S. 2010 A 2d block-structured mesh partitioner for accurate flow simulations on non-rectangular geometries. *Comput. Fluids*, doi:10.1016/j.compfluid.2010.07.009.

AIDUN, C. K., TRIANTAFILLOPOULOS, N. G. & BENSON, J. D. 1991 Global stability of a lid-driven cavity with throughflow: Flow visualization studies. *Phys. Fluids* A **3**, 2081–2091.

ALBENSOEDER, S. & KUHLMANN, H. C. 2002*a* Linear stability of rectangular cavity flows driven by anti-parallel motion of two facing walls. *J. Fluid Mech.* **458**, 153–180.

ALBENSOEDER, S. & KUHLMANN, H. C. 2002*b* Three-dimensional instability of two counter-rotating vortices in a rectangular cavity driven by parallel wall motion. *Eur. J. Mech.* B/*Fluids* **21** (3), 307–316.

ALBENSOEDER, S. & KUHLMANN, H. C. 2003 Stability balloon for the double-lid-driven cavity flow. *Phys. Fluids* **15**, 2453–2457.

ALBENSOEDER, S. & KUHLMANN, H. C. 2006 Nonlinear three-dimensional flow in the lid-driven square cavity. *J. Fluid Mech.* **569**, 465–480.

ALBENSOEDER, S., KUHLMANN, H. C. & RATH, H. J. 2001*a* Multiplicity of steady two-dimensional flows in two-sided lid-driven cavities. *Theor. Comput. Fluid Dyn.* **14**, 223–241.

ALBENSOEDER, S., KUHLMANN, H. C. & RATH, H. J. 2001*b* Three-dimensional centrifugal-flow instabilities in the lid-driven-cavity problem. *Phys. Fluids* **13**, 121–135.

BATCHELOR, G. K. 1956 On steady laminar flow with closed streamlines at large Reynolds number. *J. Fluid Mech.* **1**, 177–190.

BOPPANA, V. B. L. & GAJJAR, J. S. B. 2010 Global flow instability in a lid-driven cavity. *Intl J. Numer. Meth. Fluids* **62** (8), 827–853.

BREZILLON, A., GIRAULT, G. & CADOU, J. M. 2010 A numerical algorithm coupling a bifurcating indicator and a direct method for the computation of Hopf bifurcation points in fluid mechanics. *Comput. Fluids* **39** (7), 1226–1240.

BURGGRAF, O. R. 1966 Analytical and numerical studies of the structure of steady separated flows. *J. Fluid Mech.* **24**, 113–151.

DARR, J. H. & VANKA, S. P. 1991 Separated flow in a driven trapezoidal cavity. *Phys. Fluids* A **3**, 385–392.

DEVILLE, M., LÊ, T.-H & MORCHOISNE, Y. 1992 Numerical simulation of 3-D incompressible unsteady viscous laminar flows. *Notes on Numerical Fluid Mechanics*, vol. 36, Vieweg, Braunschweig.

DING, Y. & KAWAHARA, M. 1998 Linear stability of incompressible flow using a mixed finite element method. *J. Comput. Phys.* **139**, 243–273.

ERTURK, E. & GOKCOL, O. 2007 Fine grid numerical solutions of triangular cavity flow. *Eur. Phys. J. Appl. Phys.* **38**, 97–105.

FELDMAN, Y. & GELFGAT, A. Y. 2010 Oscillatory instability of a 3d lid-driven flow in a cube. *Phys. Fluids* **22**, 093602.

FREITAS, C. J., STREET, R. L., FINDIKAKIS, A. N. & KOSEFF, J. R. 1985 Numerical simulation of three-dimensional flow in a cavity. *Intl J. Numer. Meth. Fluids* **5**, 561–575.

GASKELL, P. H., THOMPSON, H. M. & SAVAGE, M. D. 1999 A finite element analysis of steady viscous flow in triangular cavities. *Proc. Inst. Mech. Engng C: J. Mech. Engng Sci.*, **213**, 263–276.

GHIA, U., GHIA, K. N. & SHIN, C. T. 1982 High-Re solutions for incompressible flow using the Navier--Stokes equations and a multigrid method. *J. Comput. Phys.* **48**, 387–411.

GIANNETTI, F., LUCHINI, P. & MARINO, L. 2009 Linear stability analysis of three-dimensional lid-driven cavity flow. In *Atti del XIX Congresso AIMETA di Meccanica Teorica e Applicata*, 14–17 Sep. 2009. Ancona, Italy.

GIANNETTI, F., LUCHINI, P. & MARINO, L. 2010 Characterization of the three-dimensional instability in a lid-driven cavity by an adjoint based analysis. In *Proceedings of the Seventh IUTAM Symposium on Laminar-Turbulent Transition*, Stockholm, Sweden, pp. 165–170.

GONZÁLEZ, L. M. & BERMEJO, R. 2005 A semi-langrangian level set method for incompressible Navier–Stokes equations with free surface. *Intl J. Numer. Meth. Fluids* **49**, 1111–1146.

GONZÁLEZ, L. M., THEOFILIS, V. & GÓMEZ-BLANCO, R. 2007 Finite-element numerical methods for viscous incompressible BiGlobal linear instability analysis on unstructured meshes. *AIAA J.* **45**, 840–854.

GUJ, G. & STELLA, F. 1993 A vorticity–velocity method for the numerical solution of 3-d incompressible flows. *J. Comput. Phys.* **106**, 286–298.

HILL, D. C. 1992 A theoretical approach for the restabilization of wakes. In *30th AIAA Aerospace Sciences Meeting and Exhibit*, Reno, NV, AIAA Paper 92-0067.

HILL, D. C. 1995 Adjoint systems and their role in the receptivity problem for boundary layers. *J. Fluid Mech.* **292**, 183–204.

HINATSU, M. & FERZIGER, J. H. 1991 Numerical computation of unsteady incompressible flow in complex geometry using a composite multigrid technique. *Intl J. Numer. Meth. Fluids* **13** (8), 971–997.

HUMPHREY, J. A. C., CUSHNER, J., AL-SHANNAG, M., HERRERO, J. & GIRALT, F. 2003 Shear-driven flow in a toroid of square cross section. *ASME J. Fluids Engng* **125**, 130–137.

JYOTSNA, R. & VANKA, S. P. 1995 Multigrid calculation of steady, viscous flow in a triangular cavity. *J. Comput. Phys.* **122**, 107–117.

KAWAGUTI, M. 1961 Numerical solution of the Navier–Stokes equations for the flow in a two-dimensional cavity. *J. Phys. Soc. Japan* **16**, 2307–2315.

KOSEFF, J. R. & STREET, R. L. 1984*a* The lid-driven cavity flow: A synthesis of qualitative and quantitative observations. *J. Fluids Engng* **106** (4), 390–398.

KOSEFF, J. R. & STREET, R. L. 1984*b* On end wall effects in a lid-driven cavity flow. *J. Fluids Engng* **106** (4), 385–389.

KOSEFF, J. R., STREET, R. L., GRESHO, P. M., UPSON, C. D., HUMPHREY, J. A. C. & TO, W. M. 1983 Three-dimensional lid-driven cavity flow: experiment and simulation. In *International Conference on Numerical Methods in Laminar and Turbulent Flow*, 8 Aug., Seattle, WA.

KU, H. C., HIRSCH, R. S. & TAYLOR, T. D. 1987 A pseudospectral method for solution of the three-dimensional incompressible Navier–Stokes equations. *J. Comput. Phys.* **70** (2), 439–462.

KUHLMANN, H. C., WANSCHURA, M. & RATH, H. J. 1997 Flow in two-sided lid-driven cavities: non-uniqueness, instabilities, and cellular structures. *J. Fluid Mech.* **336**, 267–299.

LERICHE, E. 2006 Direct numerical simulation in a lid-driven cubical cavity at high Reynolds number by a Chebyshev spectral method. *J. Sci. Comput.* **27** (1–3), 335–345.

LERICHE, E. & GAVRILAKIS, S. 2000 Direct numerical simulation of the flow in a lid-driven cubical cavity. *Phys. Fluids* **12** (6), 1363–1376.

LERICHE, E., GAVRILAKIS, S. & DEVILLE, M. O. 1998 Direct simulation of the lid-driven cavity flow with Chebyshev polynomials. In *Proceedings of the 4th European Computational Fluid Dynamics Conference* (ed. K. D. Papailiou), vol. 1(1), pp. 220–225. Athens, Greece.

LI, M. & TANG, T. 1996 Steady viscous flow in a triangular cavity by efficient numerical techniques. *Comput. Maths Applics.* **31**, 55–65.

LUCHINI, P. 1991 A deferred-correction multigrid algorithm based on a new smoother for the Navier–Stokes equations. *J. Comput. Phys.* **92** (2), 349–368.

MCQUAIN, W. D., RIBBENS, C. J., WANG, C.-Y. & WATSON, L. T. 1994 Steady viscous flow in a trapezoidal cavity. *Comput. Fluids* **23**, 613–626.

MOFFAT, H. K. 1963 Viscous and resistive eddies near a sharp corner. *J. Fluid Mech.* **18**, 1–18.

NITHIARASU, P. & LIU, C.-B. 2005 Steady and unsteady incompressible flow in a double driven cavity using the artificial compressibility (AC)-based characteristic-based split (CBS) scheme. *Intl J. Numer. Meth. Engng* **63**, 380–397.

OOSTERLEE, C. W., WESSELING, P., SEGAL, A. & BRAKKEE, E. 1993 Benchmark solutions for the incompressible Navier–Stokes equations in general coordinates on staggered grids. *Intl J. Numer. Meth. Fluids* **17**, 301–321.

PAN, F. & ACRIVOS, A. 1967 Steady flows in rectangular cavities. *J. Fluid Mech.* **28**, 643–655.

PERNG, C. Y. & STREET, R. L. 1991 A coupled multigrid-domain-splitting technique for simulating incompressible flows in geometrically complex domains. *Intl J. Numer. Meth. Fluids* **13** (3), 269–286.

POLIASHENKO, M. & AIDUN, C. K. 1995 A direct method for computation of simple bifurcations. *J. Comput. Phys.* **121** (2), 246–260.

PRASAD, A. K. & KOSEFF, J. R. 1989 Reynolds number and end-wall effects on a lid-driven cavity flow. *Phys. Fluids* A **1**, 208–218.

RHEE, H. S., KOSEFF, J. R. & STREET, R. L. 1984 Flow visualization of a recirculating flow by rheoscopic liquid and liquid crystal techniques. *Exp. Fluids* **2** (2), 57–64.

RIBBENS, C. J., WANG, C.-Y., WATSON, L. T. & ALEXANDER, K. A. 1991 Vorticity induced by a moving elliptic belt. *Comput. Fluids* **20**, 111–119.

RIBBENS, C. J., WATSON, L. T. & WANG, C.-Y. 1994 Steady viscous flow in a triangular cavity. *J. Comput. Phys.* **112**, 173–181.

SAAD, Y. 1980 Variations of Arnoldi's method for computing eigenelements of large unsymmetric matrices. *Linear Algebr. Applics.* **34**, 269–295.

SCHREIBER, R. & KELLER, H.B. 1983 Driven cavity flows by efficient numerical techniques. *J. Comput. Phys.* **49**, 310–333.

SHANKAR, P. N. & DESHPANDE, M. D. 2000 Fluid mechanics in the driven cavity. *Annu. Rev. Fluid Mech.* **32**, 93–136.

SIEGMANN-HEGERFELD, T., ALBENSOEDER, S. & KUHLMANN, H. C. 2007 Experiments on the transition to three-dimensional flow structures in two-sided lid-driven cavities. *Proc. Appl. Math. Mech.* **7**, 3050001 (1–2).

SIEGMANN-HEGERFELD, T., ALBENSOEDER, S. & KUHLMANN, H. C. 2008 Two- and three-dimensional flows in nearly rectangular cavities driven by collinear motion of two facing walls. *Exp. Fluids* **45**, 781–796.

SIMUNI, L. M. 1965 Numerical solution of the problem of the motion of a fluid in a rectangular hole. *J. Appl. Mech. Tech. Phys.* **6**, 106–108.

THEOFILIS, V. 2000 Globally unstable basic flows in open cavities. In *Sixth AIAA Aeroacoustics Conference and Exhibit*, Lahaina, HI, AIAA Paper 2000-1965.

THEOFILIS, V. 2003 Advances in global linear instability analysis of nonparallel and three-dimensional flows. *Prog. Aero. Sci.* **39**, 249–315.

THEOFILIS, V. 2011 Global linear instability. *Annu. Rev. Fluid Mech.* **43**, 319–352.

VERSTAPPEN, R. W. C. P. & VELDMAN, A. E. P. 1994 Direct numerical simulation of a 3D turbulent flow in a driven cavity at $Re = 10\,000$. In *Proceedings of Second Fluids Dynamics Conference*, ECCOMAS, p. 558. Stuttgart, Germany.

DE VICENTE, J., RODRIGUEZ, D., THEOFILIS, V. & VALERO, E. 2010*a* On high-Re numerical solutions in spanwise-periodic lid-driven cavity flows with complex cross-sectional profiles, doi:10.1016/j.compfluid.2010.09.033.

DE VICENTE, J., THEOFILIS, V. & VALERO, E. 2010*b* Multi-domain spectral collocation for BiGlobal instability analysis on non-conforming Cartesian subdomains. *Euro. J. Mech./B Fluids* (submitted).

VYNNYCKY, M. & KIMURA, S. 1994 An investigation of recirculating flow in a driven cavity. *Phys. Fluids* **6**, 3610–3620.

ZHOU, Y. C., PATNAIK, B. S. V., WAN, D. C. & WEI, G. W. 2003 DSC solution for flow in a staggered double lid driven cavity. *Intl J. Numer. Meth. Engng* **57**, 211–234.